Variable Eddington Factor Method for the S_N Equations with Lumped Discontinuous Galerkin Spatial Discretization Coupled to a Drift-Diffusion Acceleration Equation with Mixed Finite-Element Discretization

Samuel S. Olivier, Jim E. Morel

Department of Nuclear Engineering

Texas A&M University
College Station, TX 77843

Abstract

We apply the Variable Eddington Factor (VEF) acceleration method to the 1-D, one-group S_N equations with a Lumped Linear Discontinuous Galerkin (LLDG) spatial discretization in conjunction with a drift-diffusion acceleration equation discretized with the constant-linear Mixed Finite-Element Method (MFEM). While the VEF method is quite old, its application to this particular combination of S_N and drift-diffusion discretizations is new. In addition to demonstrating the basic properties of our method, we investigate slope reconstruction techniques for improving the consistency between the S_N and drift-diffusion solutions.

Keywords

Variable Eddington Factor, Source Iteration Acceleration, Lumped Linear Discontinuous Galerkin, Mixed Finite Element Method

Running Head

Variable Eddington Factor Method

Corresponding Author

Samuel S. Olivier, email: *smsolivier@gmail.com*.

1   Introduction

The Variable Eddington Factor (VEF) method, also known as Quasi-Diffusion (QD), was one of the first nonlinear methods for accelerating source iterations in S_N calculations [1, 2, 3]. It is comparable in effectiveness to both linear and nonlinear forms of Diffusion Synthetic Acceleration (DSA), but it offers much more flexibility than DSA. Stability can only be guaranteed with DSA if the diffusion equation is differenced in a manner consistent with that of the S_N equations [4]. Modern S_N codes often use advanced discretization schemes such as Discontinuous Galerkin (DG) since classic discretization schemes such as step and diamond are not suitable for radiative transfer calculations in the High Energy Density Laboratory Physics (HEDLP) regime or for coupled electron-photon calculations. Diffusion discretizations consistent with DG S_N discretizations generally cannot be expressed in diffusion form, but rather must be expressed in first-order or P_1 form, and are much more difficult to solve than standard diffusion discretizations [5]. Considerable effort has gone into the development of "partially consistent" diffusion discretizations that yield a stable DSA algorithm with some degree of degraded effectiveness, but such discretizations are also generally difficult to develop [6, 7, 8].

A great advantage of the VEF method is that the drift-diffusion equation that accelerates the S_N source iterations can be discretized in any valid manner without concern for consistency with the S_N discretization. When the VEF drift-diffusion equation is discretized in a way that is "non-consistent," the S_N and VEF drift-diffusion solutions for the scalar flux do not necessarily become identical when the iterative process converges. However, they do become identical in the limit as the spatial mesh is refined, and the difference between the two solutions is proportional to the spatial truncation errors associated with the S_N and drift-diffusion discretizations. In general, the order accuracy of the S_N and VEF drift-diffusion

1

solutions will be the lowest order accuracy of their respective independent discretizations. Although the S$_N$ solution obtained with such a "non-consistent" VEF method is not conservative, the VEF drift-diffusion solution is in fact conservative. This is particularly useful in multiphysics calculations where the low-order drift-diffusion equation can be coupled to the other physics components rather than the high-order S$_N$ equations. Another advantage of the non-consistent approach is that even if the S$_N$ spatial discretization scheme does not preserve the thick diffusion limit [9] when applied in isolation, that limit will generally be preserved using the VEF method.

The purpose of this paper is to investigate the application of the VEF method to the 1-D S$_N$ equations discretized with the Lumped Linear Discontinuous Galerkin (LLDG) method and the drift-diffusion equation discretized using the constant-linear Mixed Finite-Element Method (MFEM) [10]. The pairing of discontinuous and continuous finite-elements through the VEF method has been investigated before [11, 12] and a finite-element discretization of the VEF equations was developed in [13]. However, to our knowledge, this specific combination has not been previously investigated. Our motivation for this investigation is that MFEM methods are now being used for high-order hydrodynamics calculations [14]. A radiation transport method compatible with MFEM methods is clearly desirable for developing an MFEM radiation-hydrodynamics code. Such a code would combine thermal radiation transport with hydrodynamics. However, MFEM methods are inappropriate for the standard first-order form of the transport equation. Thus, the use of the VEF method with a DG S$_N$ discretization and a MFEM drift-diffusion discretization suggests itself. Only the drift-diffusion equation would be directly coupled to the hydrodynamics equations.

Here we define a VEF method that should exhibit second-order accuracy since both the transport and drift-diffusion discretizations are second-order accurate in isolation. In

addition, our VEF method should preserve the thick diffusion limit, which is essential for radiative transfer calculations in the HEDLP regime. We use the lumped rather than the standard Linear Discontinuous Galerkin discretization because lumping yields a much more robust scheme, and robustness is essential for radiative transfer calculations in the HEDLP regime. Because this is an initial study, we simplify the investigation by considering only the one-group neutron transport equation rather than the full radiative transfer equations, which include a material temperature equation as well as the radiation transport equation. Most of the relevant properties of a VEF method for radiative transfer can be tested with an analogous method for one-group neutron transport. Furthermore, a high-order DG-MFEM VEF method could be of interest for neutronics in addition to radiative transfer calculations. A full investigation for radiative transfer calculations will be carried out in a future study.

The remainder of this paper is organized as follows. First, we describe the VEF method analytically. Then, we describe our discretized S_N equations, followed by a description of the discretized VEF drift-diffusion equation. Methods for increased consistency between LLDG and MFEM are also presented. We next give computational results. In particular, we show the acceleration properties of the VEF method; compare the convergence rates of unaccelerated Source Iteration, the VEF method, and consistently-differenced S_2-synthetic acceleration (S_2SA); present the numerically-determined order of accuracy of our VEF method; compare the S_N and drift-diffusion solutions as the mesh is refined; and show that our VEF method preserves the thick diffusion limit. Finally, we give conclusions and recommendations for future work.

2 The VEF Method

2.1 The Algorithm

Here, we describe the VEF method for a planar geometry, fixed-source problem:

$$\mu \frac{\partial \psi}{\partial x}(x, \mu) + \sigma_t(x)\psi(x, \mu) = \frac{\sigma_s(x)}{2} \int_{-1}^{1} \psi(x, \mu') \, \mathrm{d}\mu' + \frac{Q(x)}{2}, \tag{1}$$

where μ is the x–axis cosine of the direction of neutron flow, $\sigma_t(x)$ and $\sigma_s(x)$ are the total and scattering macroscopic cross sections, $Q(x)$ is the isotropic fixed-source and $\psi(x, \mu)$ is the angular flux. Applying the Discrete Ordinates (S_N) angular discretization yields the following set of N coupled, ordinary differential equations:

$$\mu_n \frac{\mathrm{d}\psi_n}{\mathrm{d}x}(x) + \sigma_t(x)\psi_n(x) = \frac{\sigma_s(x)}{2}\phi(x) + \frac{Q(x)}{2}, \quad 1 \leq n \leq N, \tag{2}$$

where $\psi_n(x) = \psi(x, \mu_n)$ is the angular flux due to neutrons with directions in the cone defined by μ_n. The μ_n are given by an N-point Gauss quadrature rule such that the scalar flux, $\phi(x)$, is numerically integrated as follows:

$$\phi(x) = \sum_{n=1}^{N} w_n \psi_n(x), \tag{3}$$

where w_n is the quadrature weight corresponding to μ_n.

The VEF method begins by solving Eq. 2 while lagging the scattering source. This is called a Source Iteration (SI), and is represented as follows:

$$\mu_n \frac{\mathrm{d}}{\mathrm{d}x}\psi_n^{\ell+1/2}(x) + \sigma_t(x)\psi_n^{\ell+1/2}(x) = \frac{\sigma_s(x)}{2}\phi^\ell(x) + \frac{Q(x)}{2}, \quad 1 \leq n \leq N, \tag{4}$$

where ℓ is the iteration index. The scalar flux used in the scattering source, ϕ^ℓ, is assumed to be known either from the previous iteration or from the initial guess if $\ell = 0$. The use of a half-integral index indicates that SI is the first of a two-step iteration scheme. If one is only doing SI without acceleration, the second step would simply be to set the final scalar flux iterate to the iterate after the source iteration:

$$\phi(x)^{\ell+1} = \phi(x)^{\ell+1/2} \,. \tag{5}$$

However, SI is slow to converge in optically thick and highly scattering systems. This is the motivation for accelerating SI using the VEF method.

The second iterative step of the VEF method is to obtain a final "accelerated" iterate for the scalar flux by solving the VEF drift-diffusion equation using angular flux shape information from the source iteration step:

$$-\frac{\mathrm{d}}{\mathrm{d}x}\frac{1}{\sigma_t(x)}\frac{\mathrm{d}}{\mathrm{d}x}\left[\langle\mu^2\rangle^{\ell+1/2}(x)\phi^{\ell+1}(x)\right] + \sigma_a(x)\phi^{\ell+1}(x) = Q(x)\,, \tag{6}$$

where the Eddington factor is given by

$$\langle\mu^2\rangle^{\ell+1/2}(x) = \frac{\int_{-1}^{1}\mu^2\psi^{\ell+1/2}(x,\mu)\,\mathrm{d}\mu}{\int_{-1}^{1}\psi^{\ell+1/2}(x,\mu)\,\mathrm{d}\mu}\,. \tag{7}$$

While transport-consistent boundary conditions must be defined for Eq. 6, there is not a unique way to do this. Thus, we postpone discussion of the boundary conditions to Sec. 2.3. Note that the Eddington factor depends only upon the angular shape of the angular flux, and not its magnitude. This drift-diffusion equation is derived by first taking the first two

angular moments of Eq. 2:

$$\frac{\mathrm{d}}{\mathrm{d}x}J(x) + \sigma_a(x)\phi(x) = Q(x)\,, \tag{8a}$$

$$\frac{\mathrm{d}}{\mathrm{d}x}\left[\langle\mu^2\rangle(x)\phi(x)\right] + \sigma_t(x)J(x) = 0\,, \tag{8b}$$

where $J(x)$ is the current and the fixed source has been assumed to be isotropic. Then Eq. 8b is solved for $J(x)$, and this expression is then substituted into Eq. 8a. Performing a SI, computing the Eddington factor from the SI angular flux iterate, and then solving the drift-diffusion equation to obtain a new scalar flux iterate completes one accelerated iteration. These iterations are repeated until convergence of the scalar flux at step $\ell + 1$ is achieved. The fluxes at steps $\ell + 1/2$ and $\ell + 1$ will individually converge, but not necessarily to each other unless the S_N and drift-diffusion equations are consistently differenced or the spatial truncation error is negligible.

Acceleration occurs because the angular shape of the angular flux, and thus the Eddington factor, converges much faster than the scalar flux. In addition, the solution of the drift-diffusion equation includes scattering. This inclusion compensates for lagging the scattering source in the SI step.

The VEF method allows the S_N equations and drift-diffusion equations to be solved with arbitrarily different spatial discretization methods. The following sections present the application of the Lumped Linear Discontinuous Galerkin (LLDG) spatial discretization to the S_N equations and the constant-linear Mixed Finite-Element Method (MFEM) to the VEF drift-diffusion equation.
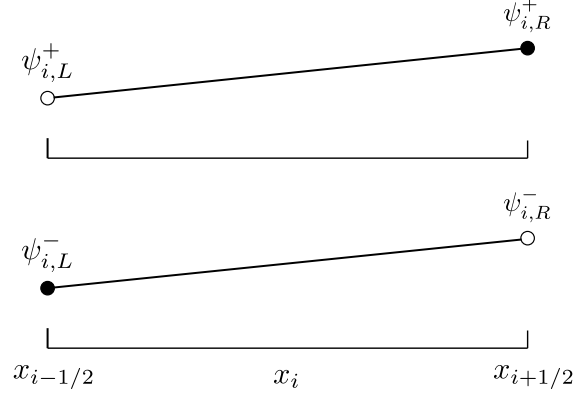
Figure 1: The distribution of unknowns within an LLDG cell. The superscript $+$ and $-$ indicate the angular fluxes for $\mu_n > 0$ and $\mu_n < 0$, respectively.

2.2   Lumped Linear Discontinuous Galerkin $\mathbf{S}_N$

The spatial grid and distribution of unknowns for an LLDG cell are shown in Fig. 1. We assume a computational domain of length x_b discretized into I cells. The indices for cell centers are integral and the indices for cell edges are half integral. The two unknowns for discrete angle μ_n within cell i are the left and right angular fluxes, $\psi_{n,i,L}^{\ell+1/2}$ and $\psi_{n,i,R}^{\ell+1/2}$. The angular flux dependence within cells is linear and is given in cell i by

$$\psi_{n,i}^{\ell+1/2}(x) = \psi_{n,i,L}^{\ell+1/2} B_{i,L}(x) + \psi_{n,i,R}^{\ell+1/2} B_{i,R}(x)\,, \quad x \in (x_{i-1/2}, x_{i+1/2}), \tag{9}$$

where

$$B_{i,L}(x) = \begin{cases} \frac{x_{i+1/2}-x}{x_{i+1/2}-x_{i-1/2}}\,, & x \in [x_{i-1/2}, x_{i+1/2}] \\[2mm] 0\,, & \text{otherwise} \end{cases}, \tag{10a}$$

$$B_{i,R}(x) = \begin{cases} \frac{x-x_{i-1/2}}{x_{i+1/2}-x_{i-1/2}}\,, & x \in [x_{i-1/2}, x_{i+1/2}] \\[2mm] 0\,, & \text{otherwise} \end{cases}, \tag{10b}$$

7

are the LLDG basis functions. The cell centered angular flux is the average of the left and right discontinuous edge fluxes:

$$\psi_{n,i}^{\ell+1/2} = \frac{1}{2}\left(\psi_{n,i,L}^{\ell+1/2} + \psi_{n,i,R}^{\ell+1/2}\right). \tag{11}$$

The interface or cell-edge fluxes are uniquely defined by upwinding:

$$\psi_{n,i-1/2}^{\ell+1/2} = \begin{cases} \psi_{n,i-1,R}^{\ell+1/2}, & \mu_n > 0 \\ \psi_{n,i,L}^{\ell+1/2}, & \mu_n < 0 \end{cases}, \tag{12a}$$

$$\psi_{n,i+1/2}^{\ell+1/2} = \begin{cases} \psi_{n,i,R}^{\ell+1/2}, & \mu_n > 0 \\ \psi_{n,i+1,L}^{\ell+1/2}, & \mu_n < 0 \end{cases}. \tag{12b}$$

The fixed source is also assumed to be linear within each cell:

$$Q_i(x) = Q_{i,L}B_{i,L}(x) + Q_{i,R}B_{i,R}(x), \quad x \in [x_{i-1/2}, x_{i+1/2}], \tag{13}$$

Because there is no spatial derivative of the fixed source, there is no need to uniquely define the fixed sources on the cell edges.

The unlumped Linear Discontinuous Galerkin discretization for Eq. 4 is obtained by substituting $\psi_{n,i}^{\ell+1/2}(x)$ from Eq. 9 and $Q_i(x)$ from Eq. 13 into Eq. 4, sequentially multiplying the resultant equation by each basis function, and integrating over each cell with integration by parts of the spatial derivative term. The lumped discretization equations are obtained simply by performing all volumetric integrals (after formal integration by parts of the spatial derivative term) using trapezoidal-rule quadrature. The LLDG discretization of Eq. 4 is given

by:

$$\mu_n \left(\psi_{n,i}^{\ell+1/2} - \psi_{n,i-1/2}^{\ell+1/2} \right) + \frac{\sigma_{t,i}h_i}{2} \psi_{n,i,L}^{\ell+1/2} = \frac{\sigma_{s,i}h_i}{4} \phi_{i,L}^{\ell} + \frac{h_i}{4} Q_{i,L} , \tag{14a}$$

$$\mu_n \left(\psi_{n,i+1/2}^{\ell+1/2} - \psi_{n,i}^{\ell+1/2} \right) + \frac{\sigma_{t,i}h_i}{2} \psi_{n,i,R}^{\ell+1/2} = \frac{\sigma_{s,i}h_i}{4} \phi_{i,R}^{\ell} + \frac{h_i}{4} Q_{i,R} , \tag{14b}$$

where h_i, $\sigma_{t,i}$, $\sigma_{s,i}$, and $Q_{i,L/R}$ are the cell width, total cross section, scattering cross section, and fixed sources in cell i. The discontinuous scalar fluxes, $\phi_{i,L/R}^{\ell}$, are assumed to be known from the drift-diffusion step of the previous iteration or the initial guess when $\ell = 0$. Equations 11, 12a, 12b, 14a, and 14b can be combined and rewritten as follows

$$\begin{bmatrix} \mu_n + \sigma_{t,i}h_i & \mu_n \\ -\mu_n & \sigma_{t,i} + \mu_n \end{bmatrix} \begin{bmatrix} \psi_{n,i,L}^{\ell+1/2} \\ \psi_{n,i,R}^{\ell+1/2} \end{bmatrix} = \begin{bmatrix} \frac{\sigma_{s,i}h_i}{2} \phi_{i,L}^{\ell} + \frac{h_i}{2} Q_{i,L} + 2\mu_n \psi_{n,i-1,R}^{\ell+1/2} \\ \frac{\sigma_{s,i}h_i}{2} \phi_{i,R}^{\ell} + \frac{h_i}{2} Q_{i,R} \end{bmatrix} , \tag{15}$$

for sweeping from left to right ($\mu_n > 0$) and

$$\begin{bmatrix} -\mu_n + \sigma_{t,i}h_i & \mu_n \\ -\mu_n & -\mu_n + \sigma_{t,i}h_i \end{bmatrix} \begin{bmatrix} \psi_{n,i,L}^{\ell+1/2} \\ \psi_{n,i,R}^{\ell+1/2} \end{bmatrix} = \begin{bmatrix} \frac{\sigma_{s,i}h_i}{2} \phi_{i,L}^{\ell} + \frac{h_i}{2} Q_{i,L} \\ \frac{\sigma_{s,i}h_i}{2} \phi_{i,R}^{\ell} + \frac{h_i}{2} Q_{i,R} - 2\mu_n \psi_{n,i+1,L}^{\ell+1/2} \end{bmatrix} , \tag{16}$$

for sweeping from right to left ($\mu_n < 0$), respectively. The right hand sides of Eqs. 15 and 16 are known as the scalar flux from the previous iteration, the fixed source, and the angular flux entering from the upwind cell are all known. By supplying the flux entering the left side of the first cell, the solution for $\mu_n > 0$ can be propagated from left to right by solving Eq. 15. Similarly, supplying the incident flux on the right boundary allows the solution for $\mu_n < 0$ to be propagated from right to left with Eq. 16. The Variable Eddington Factors
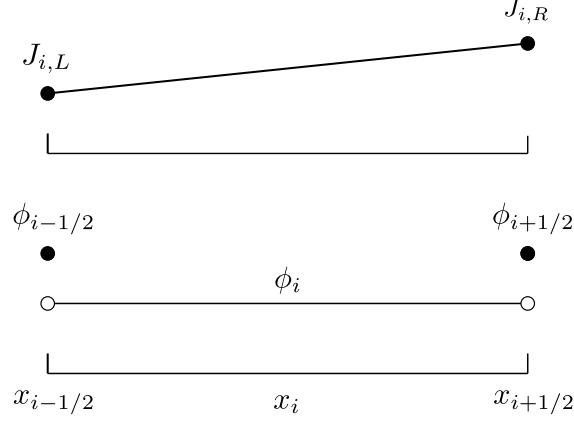
Figure 2: The distribution of unknowns in cell i for MFEM.

needed in the drift-diffusion acceleration step are computed at the cell edges as follows:

$$\langle \mu^2 \rangle_{i\pm1/2}^{\ell+1/2} = \frac{\sum_{n=1}^{N} \mu_n^2 \psi_{n,i\pm1/2}^{\ell+1/2} w_n}{\sum_{n=1}^{N} \psi_{n,i\pm1/2}^{\ell+1/2} w_n} , \tag{17}$$

where the $\psi_{n,i\pm1/2}^{\ell+1/2}$ are defined by Eqs. 12a and 12b. The Eddington factors are computed within cell i as follows:

$$\langle \mu^2 \rangle^{\ell+1/2}(x) = \frac{\sum_{n=1}^{N} \mu_n^2 \psi_n^{\ell+1/2}(x) w_n}{\sum_{n=1}^{N} \psi_n^{\ell+1/2}(x) w_n} , \quad x \in (x_{i-1/2}, x_{i+1/2}), \tag{18}$$

where $\psi_n^{\ell+1/2}(x)$ is defined by Eq. 9.

2.3 Mixed Finite-Element Method for VEF Equation

We apply the MFEM method to Eqs. 8a and 8b and then eliminate the currents to obtain a discretization for Eq. 6. In this method, the grid is identical to that used in the LLDG S_N discretization. The unknowns in an MFEM cell are depicted in Fig. 2. In MFEM, separate basis functions are used for the scalar flux and current. The scalar flux is constant within the

cell with discontinuous jumps at the cell edges and the current is a linear function defined by:

$$J_i(x) = J_{i,L}B_{i,L}(x) + J_{i,R}B_{R,i}(x) \,, \tag{19}$$

where $J_{i,L/R}$ are the currents at the left and right edges of the cell, and the basis functions are identical to those defined by Eqs. 10a and 10b for the LLDG S_N discretization. The constant-linear MFEM yields second order accuracy for both the scalar flux and the current.

The MFEM representation yields five unknowns per cell: $\phi_{i-1/2}$, ϕ_i, $\phi_{i+1/2}$, $J_{i,L}$, and $J_{i,R}$. However, each edge flux on the mesh interior is shared by two cells, so with I cells there are I cell-center scalar fluxes, $2I$ currents, $2I - 1$ interior-mesh cell-edge scalar fluxes, and 2 boundary cell-edge scalar fluxes. An equation for ϕ_i is found by integrating Eq. 8a over cell i:

$$J_{i,R} - J_{i,L} + \sigma_{a,i}h_i\phi_i = Q_ih_i \,, \tag{20}$$

where $\sigma_{a,i}$ and Q_i are the absorption cross section and source in cell i. Equations for $J_{i,L/R}$ are found by multiplying Eq. 8b by $B_{i,L/R}$ and integrating over cell i:

$$-\langle\mu^2\rangle_{i-1/2}\phi_{i-1/2} + \langle\mu^2\rangle_i\phi_i + \sigma_{t,i}h_i\left(\frac{1}{3}J_{i,L} + \frac{1}{6}J_{i,R}\right) = 0 \,, \tag{21a}$$

$$\langle\mu^2\rangle_{i+1/2}\phi_{i+1/2} - \langle\mu^2\rangle_i\phi_i + \sigma_{t,i}h_i\left(\frac{1}{6}J_{i,L} + \frac{1}{3}J_{i,R}\right) = 0 \,. \tag{21b}$$

All Eddington factors are computed using the angular fluxes from the LLDG S_N step. Note that $\langle\mu^2\rangle_{i\pm1/2}$ denotes cell edge Eddington factors, while $\langle\mu^2\rangle_i$ denotes an average over cell i of the Eddington factors. The edge Eddington factors are defined by Eq. 17, while the Eddington factors within each cell are defined by Eq. 18. We stress that evaluating Eq. 18 at $x_{i\pm1/2}$ does not yield $\langle\mu^2\rangle_{i\pm1/2}$ because of the upwinding used to define the cell edge angular

11

fluxes. The spatial dependence of the Eddington factors within each cell takes the form of a rational polynomial prompting the use of numerical quadrature to compute the average. Two point Gauss quadrature was used:

$$\langle \mu^2 \rangle_i = \frac{1}{2} \left[\langle \mu^2 \rangle (x_{i,L}^G) + \langle \mu^2 \rangle (x_{i,R}^G) \right] \tag{22}$$

where

$$x_{i,L/R}^G = \frac{x_{i+1/2} + x_{i-1/2}}{2} \mp \frac{h_i}{2\sqrt{3}} . \tag{23}$$

Eliminating $J_{i,R}$ from Eq. 21a and $J_{i,L}$ from Eq. 21b yields:

$$J_{i,L} = \frac{-2}{\sigma_{t,i} h_i} \left\{ 2 \left[\langle \mu^2 \rangle_i \phi_i - \langle \mu^2 \rangle_{i-1/2} \phi_{i-1/2} \right] - \left[\langle \mu^2 \rangle_{i+1/2} \phi_{i+1/2} - \langle \mu^2 \rangle_i \phi_i \right] \right\}, \tag{24a}$$

$$J_{i,R} = \frac{-2}{\sigma_{t,i} h_i} \left\{ 2 \left[\langle \mu^2 \rangle_{i+1/2} \phi_{i+1/2} - \langle \mu^2 \rangle_i \phi_i \right] - \left[\langle \mu^2 \rangle_i \phi_i - \langle \mu^2 \rangle_{i-1/2} \phi_{i-1/2} \right] \right\}. \tag{24b}$$

An equation for $\phi_{i+1/2}$ on the mesh interior is found by enforcing continuity of current at the cell edges:

$$J_{i,R} = J_{i+1,L} . \tag{25}$$

Using the definitions of $J_{i,L}$ and $J_{i,R}$ from Eqs. 24a and 24b in the balance equation (Eq. 20) and continuity equation (Eq. 25) yields equations for all cell-center fluxes and interior-mesh cell-edge fluxes, respectively. The resulting balance equation for cell i and continuity equation for edge $i + 1/2$ are respectively:

$$-\frac{6}{\sigma_{t,i} h_i} \langle \mu^2 \rangle_{i-1/2} \phi_{i-1/2} + \left(\frac{12}{\sigma_{t,i} h_i} \langle \mu^2 \rangle_i + \sigma_{a,i} h_i \right) \phi_i - \frac{6}{\sigma_{t,i} h_i} \langle \mu^2 \rangle_{i+1/2} \phi_{i+1/2} = Q_i h_i , \tag{26a}$$

12

and

$$-\frac{2}{\sigma_{t,i}h_i}\langle\mu^2\rangle_{i-1/2}\phi_{i-1/2} + \frac{6}{\sigma_{t,i}h_i}\langle\mu^2\rangle_i\phi_i - 4\left(\frac{1}{\sigma_{t,i}h_i} + \frac{1}{\sigma_{t,i+1}h_{i+1}}\right)\langle\mu^2\rangle_{i+1/2}\phi_{i+1/2}$$
$$+ \frac{6}{\sigma_{t,i+1}h_{i+1}}\langle\mu^2\rangle_{i+1}\phi_{i+1} - \frac{2}{\sigma_{t,i+1}h_{i+1}}\langle\mu^2\rangle_{i+3/2}\phi_{i+3/2} = 0. \quad (26b)$$

The equations for the outer boundary fluxes, $\phi_{1/2}$ and $\phi_{I+1/2}$, involve boundary conditions together with continuity conditions. For instance, the equation for $\phi_{1/2}$ is

$$J_{1,L} = J_{1/2}, \quad (27)$$

where $J_{1,L}$ is defined by Eq. 24a, and $J_{1/2}$ is the left boundary current defined by a boundary condition. For a reflective condition,

$$J_{1/2} = 0. \quad (28)$$

For a source condition,

$$J_{1/2} = 2\sum_{\mu_n>0}\mu_n\psi_{n,1/2}w_n - B_{1/2}\phi_{1/2}, \quad (29)$$

where

$$B_{1/2} = \frac{\sum_{n=1}^N|\mu_n|\psi_{n,1/2}w_n}{\sum_{n=1}^N\psi_{n,1/2}w_n} \quad (30)$$

is the boundary Eddington factor [15]. The equation for $\phi_{I+1/2}$ is

$$J_{I,R} = J_{I+1/2}. \quad (31)$$

where $J_{I,R}$ is defined by Eq. 24b, and $J_{I+1/2}$ is the right boundary current. For a reflective

condition,

$$J_{I+1/2} = 0 \, . \tag{32}$$

For a source condition,

$$J_{I+1/2} = B_{I+1/2}\phi_{I+1/2} - 2 \sum_{\mu_n < 0} |\mu_n|\psi_{n,I+1/2}w_n \, , \tag{33}$$

where

$$B_{I+1/2} = \frac{\sum_{n=1}^{N} |\mu_n|\psi_{n,I+1/2}w_n}{\sum_{n=1}^{N} \psi_{n,I+1/2}w_n} \, . \tag{34}$$

These transport-consistent, Marshak-like source boundary conditions are derived starting with the identity

$$J_{1/2} = j^+ - j^- \, , \tag{35}$$

where $j^{\pm}$ denotes the positive half-range currents associated with $\mu > 0$ and $\mu < 0$, respectively. For the left boundary condition, we simply perform the following algebraic manipulations:

$$J_{1/2} = j^+ - j^- = 2j^+ - (j^+ + j^-) = 2j^+ - \frac{j^+ + j^-}{\phi}\phi = 2j^+ - B_{1/2}\phi \, . \tag{36}$$

For the right boundary condition, we similarly obtain

$$J_{I+1/2} = j^+ - j^- = (j^+ + j^-) - 2j^- = \frac{j^+ + j^-}{\phi}\phi - 2j^- = B_{I+1/2}\phi - 2j^- \, . \tag{37}$$

Note that these source boundary conditions become equivalent to the standard Marshak boundary conditions if the S_N angular flux is isotropic. The resulting system of $2I + 1$ equations for the cell-center and cell-edge fluxes can be assembled into a matrix of both

cell-center and cell-edge scalar fluxes and solved with a banded matrix solver of bandwidth five. The resulting drift-diffusion scalar flux can either be used as the final solution if the solution has converged or as an update to the LLDG S_N scattering source. Use of these piecewise-constant fluxes to represent the LLDG S_N scattering source is the default method, and is referred to as the flat update method.

2.4   Increased Consistency Between LLDG and MFEM

The MFEM representation for the scalar flux is constant within a cell, but the LLDG representation for the scalar flux is linear. This suggests that improved accuracy of the S_N solution could be achieved by somehow constructing a linear scalar flux dependence from the MFEM solution. One simple method for doing this is to use the MFEM cell-edge scalar fluxes to compute a slope, which is then combined with the MFEM cell-center flux value to obtain a linear dependence. This works quite well for neutronics. However, it will be inadequate in a radiative transfer calculation because slopes must also be generated for the material temperatures, and an MFEM approximation for the temperatures will not include edge temperatures. We have chosen to use a more generally applicable approach based upon standard data reconstruction techniques that require only cell-centered values to compute slopes [16]. We also limit such slopes to avoid non-physical scalar fluxes. For example, the reconstructed left and right scalar fluxes in cell i are given by

$$\phi_{i,L/R} = \phi_i \mp \frac{1}{4}\xi_i \left(\Delta\phi_{i+1/2} + \Delta\phi_{i-1/2} \right) , \tag{38}$$

where ξ is a van Leer-type slope limiter [16]:

$$\xi_i = \begin{cases} 0, & r_i \leq 0 \,, \\ \min\left\{ \frac{2r_i}{1+r_i}, \frac{2}{1+r_i} \right\}, & r_i > 0 \end{cases} \,, \tag{39a}$$

$$r_i = \frac{\Delta\phi_{i-1/2}}{\Delta\phi_{i+1/2}} \,, \tag{39b}$$

and

$$\Delta\phi_{i+1/2} = \phi_{i+1} - \phi_i \,, \tag{40a}$$

$$\Delta\phi_{i-1/2} = \phi_i - \phi_{i-1} \,. \tag{40b}$$

On the boundaries, we use

$$\phi_{1,L/R} = \phi_1 \mp \frac{1}{2}\Delta\phi_{3/2} \,, \tag{41a}$$

$$\phi_{I,L/R} = \phi_I \mp \frac{1}{2}\Delta\phi_{I-1/2} \,. \tag{41b}$$

We also set any negative left or right flux values in the boundary cells to zero by appropriately rotating the slopes.

3   Computational Results

We first consider a test problem that is homogeneous with a reflecting left boundary, vacuum right boundary, and a total thickness of $10\,\text{cm}$. The total and scattering macroscopic cross sections were set to $1\,\text{cm}^{-1}$ and $0.99\,\text{cm}^{-1}$ leading to a scattering ratio of $c = \frac{\sigma_s}{\sigma_t} = 0.99$. With 50 spatial cells the optical thickness per cell was 0.2 mfp and the domain thickness

was 10 mfp. The isotropic fixed source was set to $1\,\frac{\text{particles}}{\text{s}\cdot\text{cm}^3}$. Unless otherwise indicated in this section, all calculations were performed with 50 uniform spatial cells and S_8 Gauss quadrature. In addition, the scalar flux was point-wise converged for both the left and right discontinuous fluxes according to:

$$\frac{1}{1-\rho}\,\max\left[\phi_{i,L/R}^{\ell+1}-\phi_{i,L/R}^{\ell}\right]<10^{-6}\,,\tag{42}$$

where

$$\rho=\frac{\|\phi^{\ell+1}-\phi^{\ell}\|_2}{\|\phi^{\ell}-\phi^{\ell-1}\|_2}\tag{43}$$

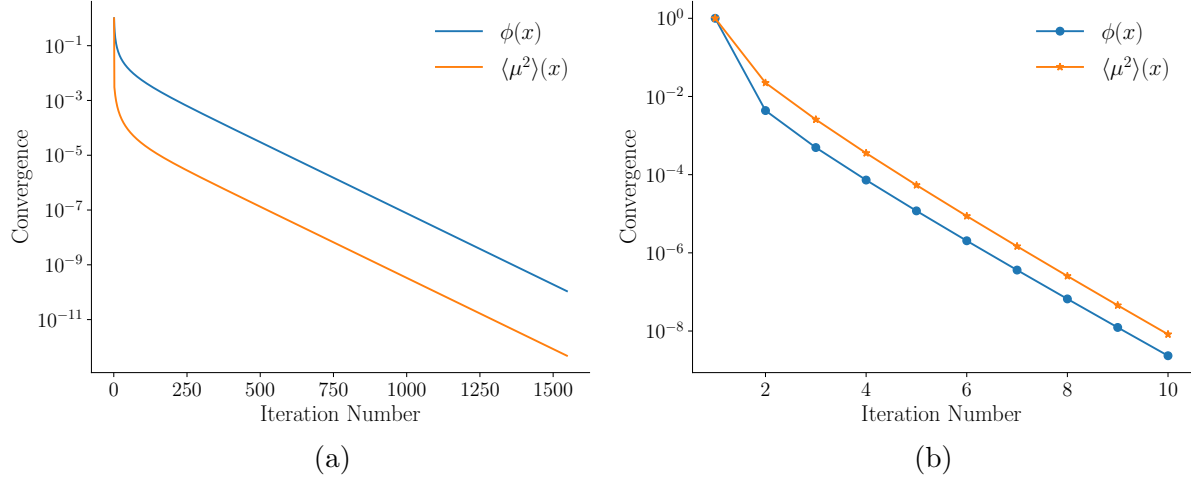is an estimate for an asymptotic error reduction factor.

Figure 3: Relative iterative change for $\phi(x)$ and $\langle\mu^2\rangle(x)$ for (a) unaccelerated and (b) VEF accelerated SI.

The relative iterative change, defined as

$$\frac{\|f^{\ell+1}-f^{\ell}\|_2}{\|f^{\ell+1}\|_2}\,,\tag{44}$$

is given in Figure 3a as a function of unaccelerated iteration number for $f = \phi(x)$ and $f = \langle \mu^2 \rangle(x)$. The relative iterative change is a crude measure of iterative convergence. The Eddington factor's large drop in relative iterative change between the first and second iterations supports the claim that the angular shape of the angular flux, and thus the Eddington factor, converges rapidly. When compared to Fig. 3b, a plot of the relative iterative change for the VEF method, it is clear that the VEF method transfers the fast rate of convergence of the Eddington factor to the scalar flux.

For the previously-described homogeneous problem, the number of iterations required for convergence of unaccelerated SI, the VEF method, and consistently-differenced S_2SA is plotted in Figure 4 for a range of scattering ratios. The ratio of unaccelerated to VEF accelerated iterations ranged from 1.6 to 267. As expected, the effectiveness of acceleration for the VEF and S_2SA methods is essentially the same.

The Method of Manufactured Solutions (MMS) was used to compare the spatial accuracy of our VEF method as the cell width was decreased. A solution to Eq. 2 was assumed as follows:

$$\psi_{n,\text{MMS}}(x) = \sin\left(\frac{\pi x}{x_b}\right)\left(1 + \mu_n \frac{2x - x_b}{x_b}\right), \quad x \in [0, x_b], \tag{45}$$

with the corresponding scalar flux given by

$$\phi_{\text{MMS}}(x) = \sum_{n=1}^{N} \psi_{n,\text{MMS}}(x) w_n = 2\sin\left(\frac{\pi x}{x_b}\right). \tag{46}$$

Note that this solution satisfies vacuum boundary conditions at $x = 0$ and $x = x_b$. Substituting this solution into the following version of Eq. 2 with a more general source,

$$\mu_n \frac{\mathrm{d}\psi_n}{\mathrm{d}x}(x) + \sigma_t(x)\psi_n(x) = \frac{\sigma_s(x)}{2}\phi(x) + Q_n(x), \quad 1 \leq n \leq N, \tag{47}$$
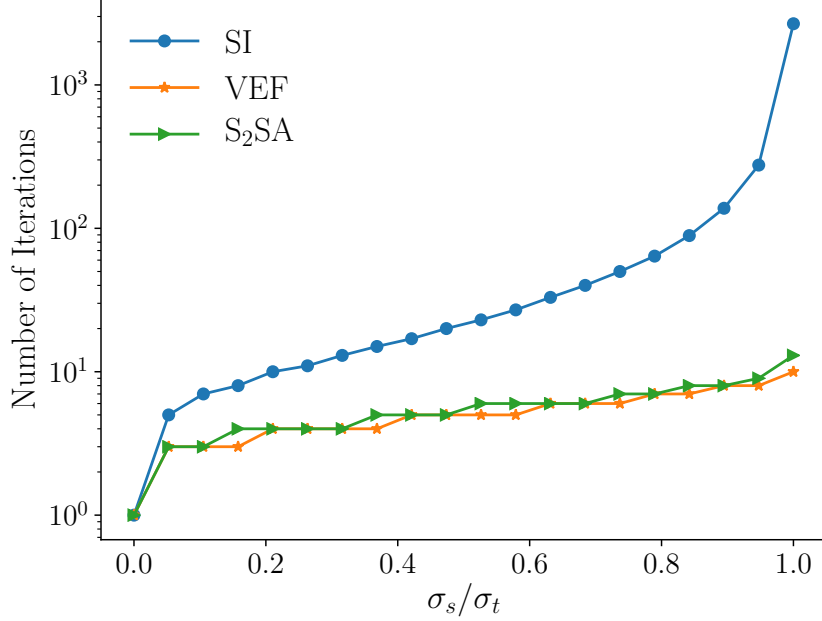
Figure 4: A comparison of the number of iterations required to converge for Source Iteration, VEF acceleration, and S$_2$SA for varying ratios of σ_s to σ_t.

and solving for $Q_n(x)$ yields:

$$Q_{n,\text{MMS}}(x) = \mu_n \left[2\frac{\mu_n}{x_b} \sin\left(\frac{\pi x}{x_b}\right) + \frac{\pi}{x_b} \cos\left(\frac{\pi x}{x_b}\right) \left(1 + \mu_n \frac{2x - x_b}{x_b}\right) \right]$$
$$+ \sigma_t(x) \sin\left(\frac{\pi x}{x_b}\right) \left(1 + \mu_n \frac{2x - x_b}{x_b}\right) - \sigma_s(x) \sin\left(\frac{\pi x}{x_b}\right) . \quad (48)$$

Using Eq. 48 as the fixed source in Eq. 47, and imposing vacuum boundary conditions at $x = 0$ and $x = x_b$ makes Eq. 45 the analytic solution of Eq. 47. Thus the difference between a numerical solution of Eq. 47 (defined in this way) and the MMS solution is the spatial truncation error of the numerical solution. Calculations were performed for the MMS problem using the cross sections of the homogeneous problem, but with vacumm

conditions at both boundaries and a slab width of $1\,\mathrm{cm}$. The L2 norm of the difference between the numerical and MMS solutions was computed for five logarithmically spaced cell widths between $0.5\,\mathrm{mm}$ and $0.01\,\mathrm{mm}$. A fit of the following form to the numerical error, E,

$$E = Ch^n \tag{49}$$

was used to determine the order of accuracy, n, and the constant of proportionality, C. These values are provided in Table 1 for the VEF method with the flat and van Leer slope reconstruction scattering source update methods. The lower C value for VEF with van Leer reconstructed slopes indicates that constructing a linear scalar flux dependence from the MFEM drift-diffusion flux increases numerical accuracy. Both methods show second-order accuracy as expected from the orders of accuracy of the LLDG and constant-linear MFEM discretizations in isolation. This indicates that while slope reconstruction can affect numerical accuracy it does not affect the order of accuracy of the method.

Update Method	Order	C	R^2
Flat	2.033	1.11	9.9983×10^{-1}
van Leer	2.017	0.594	9.9904×10^{-1}

Table 1: The order of accuracy, error, and R^2 values for flat and van Leer slope reconstruction scattering source update methods.

The difference between the S_N solution and the drift-diffusion solution was compared as a function of cell width for the homogeneous slab problem and for a heterogeneous problem. The heterogeneous problem is a modified version of Reed's problem [17]. S_2SA was used to generate the S_N solution to which the VEF method was compared. In both cases, the left boundary was reflecting and the right boundary was vacuum. The homogeneous slab had a scattering ratio of 0.99. The cross sections and sources for the heterogeneous problem

are provided in Table 2. The L2 norm of the difference between the SI solution and VEF solution is plotted for the flat and van Leer scattering source update methods in Figs. 5a and 5b for the homogeneous and heterogeneous problems, respectively.

	Region 1	Region 2	Region 3	Region 4	Region 5
Q	10	0	0	0	1
σ_t	10	0.001	1	5	1
σ_a	10	0	0.1	0	0.1
Domain	$0 \leq x < 2$	$2 \leq x < 4$	$4 \leq x < 6$	$6 \leq x < 7$	$7 \leq x \leq 8$

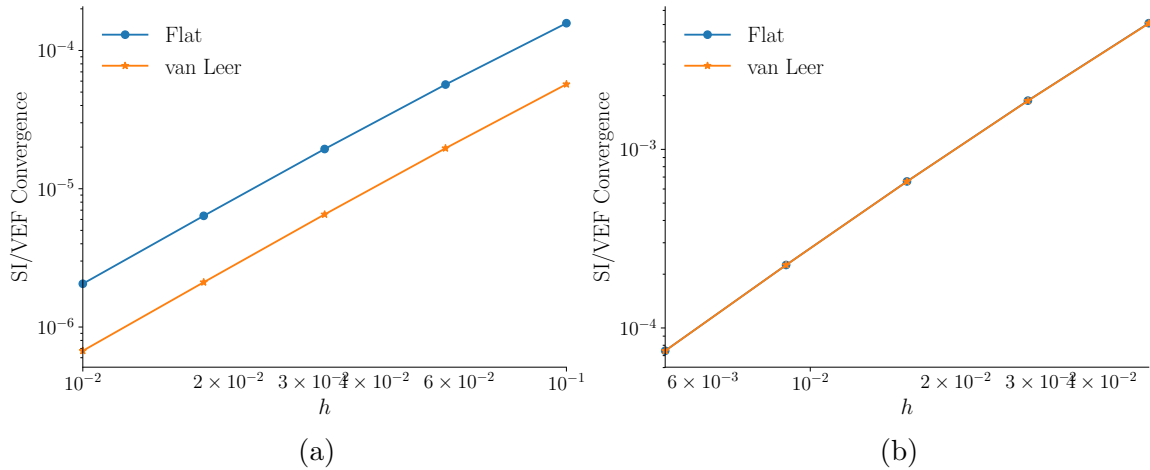Table 2: The cross sections and source used for the heterogeneous problem.

Figure 5: The L2 norm of the difference between the S_N and drift-diffusion solutions as a function of cell width for the two scattering source update methods. Results for the homogeneous problem and Reed's problem are given in (a) and (b), respectively.

In the homogeneous problem, VEF with van Leer limited slope reconstruction was three times closer to the S_N solution than VEF without reconstruction. However, in the heterogeneous problem, reconstruction did not affect the convergence of drift-diffusion to S_N. This could be due to the fact that the flux derivatives are discontinuous at material interfaces and the cell-centered slope reconstruction method has no knowledge of these discontinuities.

Lastly, the VEF method was tested in the diffusion limit. Calculations were performed for several variants of the homogeneous problem. These problems differed from the homogeneous problem only with respect to the cross sections and fixed source, which were scaled as follows [18]:

$$\sigma_t(x) \to \sigma_t(x)/\epsilon \,, \tag{50a}$$

$$\sigma_a(x) \to \epsilon\sigma_a(x) \,, \tag{50b}$$

$$Q(x) \to \epsilon Q(x) \,, \tag{50c}$$

with $\sigma_t = \sigma_a = 1 \, \text{cm}^{-1}$ and $Q = 1 \frac{\text{particles}}{\text{s} \cdot \text{cm}^3}$. As $\epsilon \to 0$, the system becomes diffusive. The number of iterations until convergence as $\epsilon \to 0$ is provided in Table 3. Figure 6 shows that the scalar fluxes from the VEF method and analytic diffusion agree for small ϵ as expected from the scaling of the cross sections and source. These results support the claim that the VEF method is robust in the diffusion limit as both scattering update methods properly preserved the thick diffusion limit.

ϵ	Flat	Linear
1.0×10^{-1}	6	6
1.0×10^{-2}	3	3
1.0×10^{-3}	2	2
1.0×10^{-4}	2	2
1.0×10^{-5}	2	2

Table 3: The number of iterations until convergence for a range of ϵ values for the flat and linear scattering update methods.
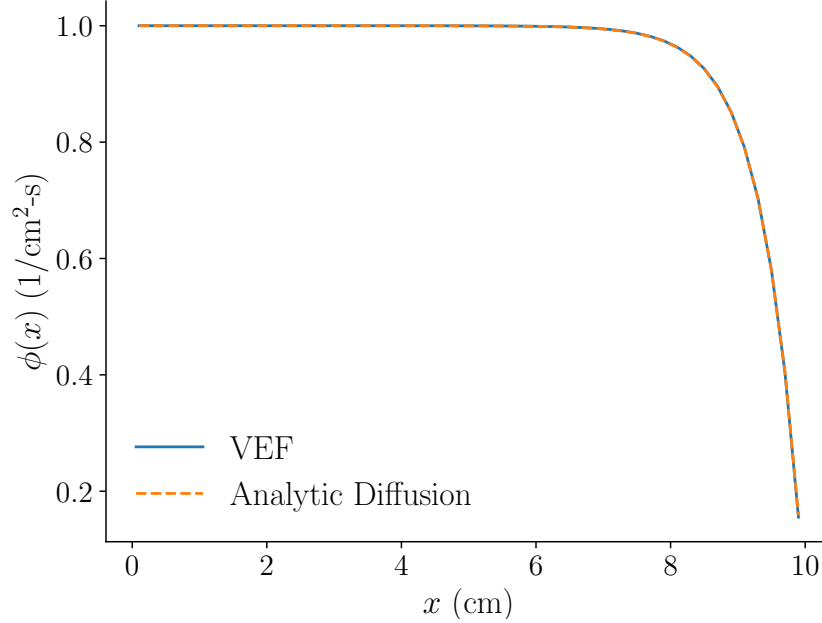
Figure 6: The scalar flux profile for the VEF solution with $\epsilon = 10^{-5}$ compared to the exact diffusion solution.

4   Conclusions and Future Work

We have presented a VEF method for the one-group slab-geometry neutron transport equation coupling S_N equations having a Lumped Linear Discontinuous Galerkin spatial discretization with a drift-diffusion equation having a constant-linear Mixed Finite-Element discretization. We have numerically demonstrated that our LLDG/MFEM VEF method is as effective as consistently-differenced S_2SA; that both the S_N and drift-diffusion equations exhibit second-order accuracy and thus approach each other with second-order accuracy as the spatial mesh is refined; and that the thick diffusion limit is preserved. We also investigated two methods for updating the S_N scattering source given the drift-diffusion solution for the scalar flux. The first was to simply use the flat scalar flux dependence of the drift-diffusion

23

solution in the S_N scattering source. The other was to reconstruct a linear discontinuous scattering source using the flat or cell-average MFEM fluxes together with standard slope reconstruction methods. For a homogeneous problems, the linear update was more accurate, but there was little difference between the flat and linear updates for a highly inhomogeneous problem. All of the desired VEF properties such as order accuracy and preservation of the diffusion limit were obtained independent of the scattering source update procedure. Most importantly, it is clear that S_N and and drift-diffusion solutions that differ in proportion to truncation error is a small price to pay for the versatility afforded by the VEF method for multiphysics calculations. The conservative drift-diffusion equation can be coupled to the other physics equations and discretized in a manner compatible with those equations. Furthermore, the difference between the S_N and drift-diffusion equations is a measure of the truncation error of the drift-diffusion solution, which is a very useful error estimator naturally provided by the VEF method.

In the future we intend to extend the VEF method presented in this paper to the radiative transfer equations, with higher order discretizations in 2-D and 3-D geometries. A major question that we intend to address in the near term is the impact of the linear scattering source update technique in radiative transfer calculations, particularly in Marshak wave problems, where slope reconstruction for the emission source is known to be important to mitigate a numerical artifact referred to as the "teleportation" effect [19].

References

[1] M.L. Adams and E.W. Larsen. Fast iterative methods for discrete-ordinates particle transport calculations. *Progress in Nuclear Energy*, 40(1):3–159, 2002.

[2] D. Mihalas. *Stellar Atmospheres*. W. H. Freeman and Co, 1978.

[3] V. Ya. Gol'din. A quasi-diffusion method of solving the kinetic equation. *USSR Comp. Math. and Math. Physics*, 4:136–149, 1964.

[4] R.E. Alcouffe. Diffusion synthetic acceleration methods for the diamond-differenced discrete-ordinates equations. *Nuclear Science and Engineering*, 64:344–355, 1977.

[5] J.S. Warsa, T.A. Wareing, and J.E. Morel. Fully-consistent diffusion-synthetic acceleration of linear discontinuous S_n transport discretizations on unstructured tetrahedral meshes. *Nuclear Science and Engineering*, 141:235–251, 2002.

[6] J.E. Morel and E.W. Larsen. A multiple balance approach for differencing the S_n equations. *Nuclear Science and Engineering*, 105:1–15, 1990.

[7] Marvin L. Adams and William R. Martin. Diffusion synthetic acceleration of discontinuous finite element transport iterations. *Nuclear Science and Engineering*, 111:145–167, 1992.

[8] Yaqi Wang and Jean C. Ragusa. Diffusion synthetic acceleration for high-order discontinuous finite element S_n transport schemes and application to locally refined unstructured meshes. *Nuclear Science and Engineering*, 166(2):145–166, 2010.

[9] Edward W. Larsen, J.E. Morel, and Warren F. Miller, Jr. Asymptotic solutions of numerical transport problems in optically thick, diffusive regimes. *Journal of Computational Physics*, 69:283–324, 1987.

[10] Raviart, P. A. and Thomas, J. M. *A mixed finite element method for 2-nd order elliptic problems*, pages 292–315. Springer Berlin Heidelberg, Berlin, Heidelberg, 1977.

[11] W.A. Wieselquist. A low-order quasidiffusion discretization via linear-continuous finite-elements on unstructured triangular meshes. Proceedings of Int. Conf. PHYSOR 2010.

[12] D.Y. Anistratov and J.S. Warsa. Dfem discretization of quasidiffusion moment equations in 1d slab geometry. Proceedings of M&C 2017 - International Conference on Mathematics and Computational Methods Applied to Nuclear Science and Engineering, Jeju, Korea, April 16-20, 2017.

[13] E.W. Larsen and Jinan Yang. A functional monte carlo method for k-eigenvalue problems. *Nuclear Science and Engineering*, 159:107–126, 2008.

[14] V. Dobrev, Tz. Kolev, and R. Rieben. High-order curvilinear finite element methods for lagrangian hydrodynamics. *SIAM Journal on Scientific Computing*, 34:B606–B641, 2012.

[15] M.M. Miften and E.W. Larsen. The quasi-diffusion method for solving transport problems in planar and spherical geometries. *Journal of Transport Theory and Statistical Physics*, 22(2-3):165–186, 1992.

[16] B. van Leer. Towards the ultimate conservative difference scheme I: The quest for monotonicity. *Lecture Notes in Physics*, 18:163–168, 1973.

[17] William H. Reed. New difference schemes for the neutron transport equation. *Nuclear Science and Engineering*, 45:309–314, 1971.

[18] Edward W. Larsen, J.E. Morel, and Jr. Warren F. Miller. Asymptotic solutions of numerical transport problems in optically thick, diffusive regimes. *Journal of Computational Physics*, 69:283–324, 1987.

[19] Adam Glenn Irvine, Ian D. Boyd, and Nicholas A. Gentile. Reducing the spatial discretization error of thermal emission in Implicit Monte Carlo simulations. *Journal of Computational and Theoretical Transport*, 45(1-2):99–122, 2016.